第 48 卷 第 16 期/2021 年 8 月/中国激光 研究论文

中国激光

面向大晶面超声换能器的虚拟平行投影光声模型重建方法

李娇[1,2*]，苗士超[1]，宋少泽[1]，路彤[1]，陈婷婷[1]，高峰[1,2]

[1]天津大学精密仪器与光电子工程学院，天津 300072；

[2]天津市生物医学检测技术与仪器重点实验室，天津 300072

摘要 在光声层析成像重建方法中，当考虑超声换能器特别是大晶面超声换能器的尺寸影响时，经典的光声模型重建算法需将晶面离散化，通过分别计算每个离散点的正向模型并求和来建立最终的正向模型矩阵。这种基于模型的重建方法已被证明比传统的延迟叠加和反投影重建方法具有更高的精确性，但同时也会导致巨大的时间消耗和计算/存储空间。本文提出了一种基于虚拟平行投影的光声模型重建方法，该方法用直接建立虚拟平行投影的模型矩阵来代替晶面离散点模型矩阵之和，适用于使用大晶面柱形聚焦或平面超声换能器的光声层析成像系统。数值模拟、仿体实验及活体实验结果表明，所提方法与基于离散化晶面的光声模型重建方法具有相似的图像重建性能，但其重建过程的时间消耗和计算/存储空间需求显著降低。

关键词 医用光学；光声层析成像；虚拟平行投影；模型重建算法

中图分类号 Q631 **文献标志码** A **doi**：10.3788/CJL202148.1607001

1 引 言

近年来，光声成像方法因结合了光学成像的高光学对比度和超声成像的高穿透特性而发展迅速。光声成像技术以超短脉冲激光作为激励源并以超声作为媒介，可以提供生物组织的结构和功能性信息[1-4]。其中，光声层析成像(PAT)技术可在不同的空间分辨率和穿透深度下实现多尺度成像[5]，成像深度可达数厘米且分辨率在百微米级别[6]，主要应用于活体小动物成像[7]、人体乳腺成像[8-9]及关节成像[10-11]等预临床及临床研究中。该技术与多光谱技术相结合的特点使其在生物组织的血氧饱和度功能性成像[12-13]及药代动力学[14]研究等生物医学领域的应用愈加广泛。

在光声成像中，超声换能器的几何特征和工作特性对重建方法的选择及重建图像质量起着关键作用。具体来说，换能器晶面的尺寸和频率响应限制了光声成像系统的灵敏度和分辨率特性[15]。为了在测量范围内获得均匀的声场响应，光声层析成像一般采用大晶面的柱形聚焦或平面超声换能器，即换能器的晶面尺寸一般远超过其空间分辨率(100～300 μm)。然而，传统的重建方法通常忽略换能器的尺寸特征，即将其近似为点探测器，这对于采用大晶面换能器的系统来说会造成不可忽略的计算误差。目前，研究中主要用两种方式来解决换能器几何尺寸带来的误差问题：1)将换能器的晶面近似成多个离散点[15-18]，分别将每个离散点作为点探测器进行模型矩阵的计算，然后求和获得最终的模型矩阵。该方法因适用于任何形状的换能器而被广泛使用。然而，晶面离散点数目的增加在提高光声图像重建质量的同时也会线性地增加时间消耗与计算/存储空间需求，即使采用 GPU 加速的重建方法也无法避免[19-20]；而柱对称方法[21]虽然能简化前向模型的计算过程从而缩短计算时间，但仅适用于具有

收稿日期：2020-12-28；**修回日期**：2021-01-28；**录用日期**：2021-02-22

基金项目：国家自然科学基金(81771880，81401453，81671728，81871393，81971656)、天津市自然科学基金(19JCQNJC12800)

通信作者：*jiaoli@tju.edu.cn

固有对称性的光声层析成像系统。2)计算换能器的空间脉冲响应(SIR)[22-24],然后将其与测量位置处的声压信号进行卷积,实现光声重建。这种方法虽然不需要对换能器晶面进行离散求和,但其预处理时间消耗及计算/存储空间需求与离散近似模型重建算法属于同一量级。

本文提出了一种面向大晶面超声换能器的虚拟平行投影光声模型重建方法,即直接采用虚拟平行投影模型矩阵作为最终的模型矩阵,以避免换能器晶面多离散点的模型矩阵计算及求和操作,从而优化运行时间并减少内存消耗。通过比较传统的模型重建方法(MB)、晶面离散近似模型重建方法(MB-SE)和虚拟平行投影模型重建方法(MB-VP)在数值模拟、仿体实验和活体小鼠实验中的重建结果,验证了三种重建方法的计算效率及重建质量等特性。实验结果表明,MB-VP 方法用最少的计算时间和计算/存储空间(与传统 MB 方法相同)就可获得与 MB-SE 方法相同的高质量重建图像。

2 基本原理

2.1 多角度片光照射模式光声层析成像系统

本课题组自主搭建的多角度片光照射模式光声层析成像系统如图 1 所示。脉冲激发光来自 Nimma-600 型 Nd:YAG 激光器泵浦的 LP604 型光学参量振荡器,波长范围为 680~1064 nm,脉冲持续时间为 6 ns,重复频率为 10 Hz。激发光耦合进入定制的四臂光纤束中,并被均匀地布置在仿体四周形成多角度宽场光照明模式。4 个单臂光纤束的出射光分别通过平凸透镜和柱面透镜进行光束整形,最终在成像目标表面形成一个高约 3 mm 的狭窄光束,即实现了多角度片光照明模式。本系统采用直径为 25 mm、中心频率为 3.5 MHz 的柱形聚焦换能器探测光声信号。成像腔连接在电动旋转台上,可保证换能器在不同角度接收光声信号。接收到的信号由 50 dB 前置放大器进行预放大,之后由 PCI8552 型数据采集卡以 75 MHz 的采样频率进行采集量化,最后传送至计算机进行存储,用于后续的图像重建。

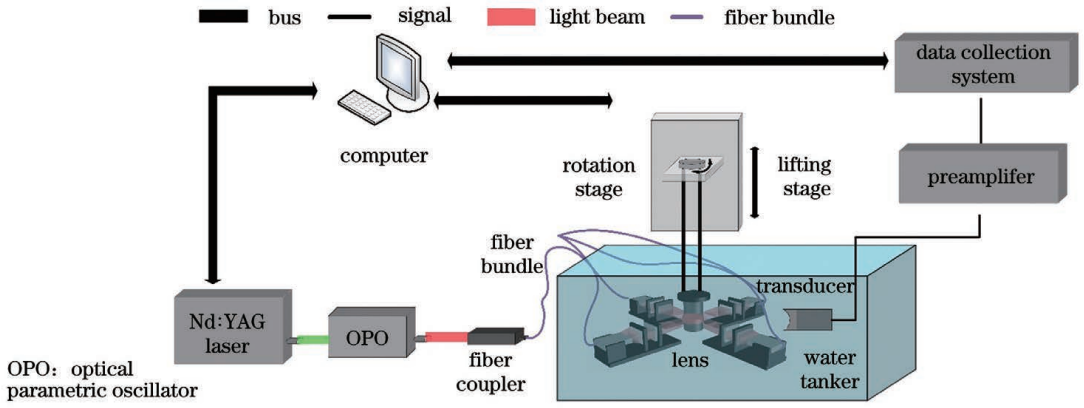

图 1 多角度片光照明模式的光声层析成像系统示意图

Fig. 1 Schematic of photoacoustic tomography system with multi-view light-sheet illuminations

2.2 基于虚拟平行投影的模型重建算法

基于光声效应及波动方程[25],位置 $\boldsymbol{r}$ 处的初始声压 $P(\boldsymbol{r},t)$ 可表示为吸收光能 $H(\boldsymbol{r})$ 的函数[17],即

$$P(\boldsymbol{r},t)=\frac{\Gamma}{4\pi c}\frac{\partial}{\partial t}\int_{S'(t)}\frac{H(\boldsymbol{r}')}{|\boldsymbol{r}-\boldsymbol{r}'|}\mathrm{d}S'(t),\quad(1)$$

式中:c 是介质中的声速;$S'(t)$ 是由 $|\boldsymbol{r}-\boldsymbol{r}'|=ct$ 定义的球面;Γ 是 Grueneisen 因子;t 是时间。当采用片光照射模式和柱形聚焦或平面超声换能器时,(1)式可以简化至二维模型

$$P(\boldsymbol{r},t)=\frac{\partial}{\partial t}\int_{L'(t)}\frac{H(\boldsymbol{r}')}{|\boldsymbol{r}-\boldsymbol{r}'|}\mathrm{d}L'(t),\quad(2)$$

空间球面 $S'(t)$ 变为圆弧上的 $L'(t)$。为了突出声压信号明显变化的部分,对时间 t 进行差分近似,即

$$P(\boldsymbol{r},t)\approx\frac{I(t+\Delta t)-I(t-\Delta t)}{2\Delta t},\quad(3)$$

其中,

$$I(t)=\int_{L'(t)}\frac{H(\boldsymbol{r}')}{|\boldsymbol{r}-\boldsymbol{r}'|}\mathrm{d}L'(t)。\quad(4)$$

在二维重建中,点探测器的反投影等值线 $L'(t)$ 是以探测器为中心的弧线,如图 2 所示,将 $L'(t)$ 近似离散化为 $M-1$ 条线段,产生如图 2 中三角形标识的 M 个离散插值点。当离散点数足够多时,用离散插值点代替离散线段,此时 $I(t)$ 被离散化为

$$I(t)\approx\frac{1}{2}\sum_{l=1}^{M}\frac{H(\boldsymbol{r})}{|\boldsymbol{r}-\boldsymbol{r}'|}(d_{l-1,l}+d_{l,l+1}),\quad(5)$$

式中:d 为两个三角形标示的离散点间的距离。

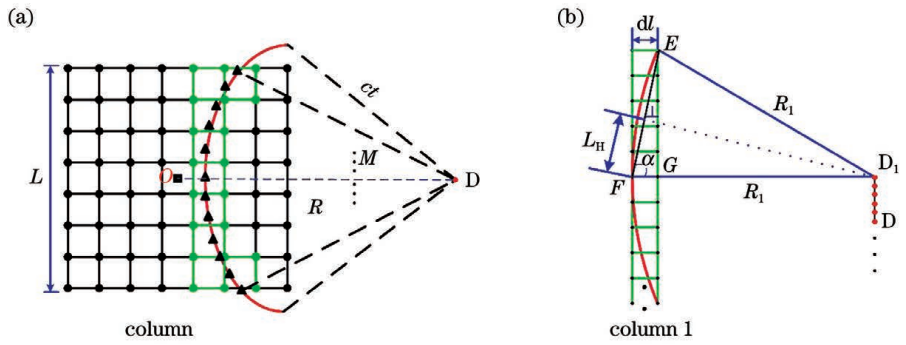

图 2　光声重建过程中正向模型的离散化及计算最小旋转半径的原理示意图。(a)正向模型的离散化;(b)计算最小旋转半径的原理示意图

Fig. 2　Discretization of the forward model in reconstruction procedures and the schematic of calculating the minimum rotation radius of the transducer. (a) Discretization of the forward model; (b) calculating the minimum rotation radius of the transducer

根据离散点与邻近重建网格像素点的距离关系,采用插值公式建立权重关系,结合(3)～(5)式和插值公式,可以得到前向模型矩阵 $\boldsymbol{A}$。对于大晶面换能器,传统的 MB 方法将探测器近似为点探测器并计算其模型矩阵,MB-SE 方法将探测器晶面各离散点的模型矩阵 $\boldsymbol{A}_i$ 求和后作为最终的前向模型矩阵 $\boldsymbol{A}_{\text{sum}}$。前向模型矩阵 $\boldsymbol{A}$ 反映了某一时刻某一位置处的声压 $\boldsymbol{P}$ 与目标重建网格点上光吸收分布 $\boldsymbol{H}$ 之间的线性关系:$\boldsymbol{P}=\boldsymbol{A}\boldsymbol{H}$。然后采用最小二乘拟合的方法(LSQR)迭代求解 $\min\|\boldsymbol{P}-\boldsymbol{A}\boldsymbol{H}\|^2$,进行图像的重建。

在先前的研究工作中,本课题组提出将“虚拟平行投影”的概念[26]引入到光声层析成像中。如图 2(b)所示,当换能器的晶面尺寸与旋转半径足够大时,D1 是换能器边缘的“虚拟点”探测器,E、F 和 G 分别是边长为 L 的重建网格的边缘点,重建网格的最小尺寸为 dl(即 F 与 G 间的距离)。如果换能器 D(尺寸为 h)反投出的等值线能够近似完全地包含于最靠近探测器位置一侧的一列重建网格 column 1 范围内,则可以近似认为此时的旋转半径 R 为满足虚拟平行投影条件的最小旋转测量半径,即

$$R \geqslant (R_1-\mathrm{d}l)+\frac{L}{2},\ R_1=\frac{\sqrt{\left(\frac{L-h}{2}\right)^2+\mathrm{d}l^2}}{2\cos\left[\arctan\left(\frac{L-h}{2\mathrm{d}l}\right)\right]}。\tag{6}$$

探测器各离散点的反投影等值线在重建区域内可近似为平行于换能器晶面的直线,如图 3(a)所示,即满足虚拟平行投影条件,此时 $L'(t)$ 上各离散点的间距是相等的,(5)式可改写为

$$I(t)\approx\sum_{l=1}^{M}\frac{H(\boldsymbol{r})}{|\boldsymbol{r}-\boldsymbol{r}'|}d_l。\tag{7}$$

如图 3(b)所示,满足虚拟平行投影条件的前向模型直接以平行线建立插值点,近似代替所有离散插值点的累加和,避免 $\boldsymbol{A}_i$ 的重复计算,降低了时间消耗以及对计算/存储空间的要求。

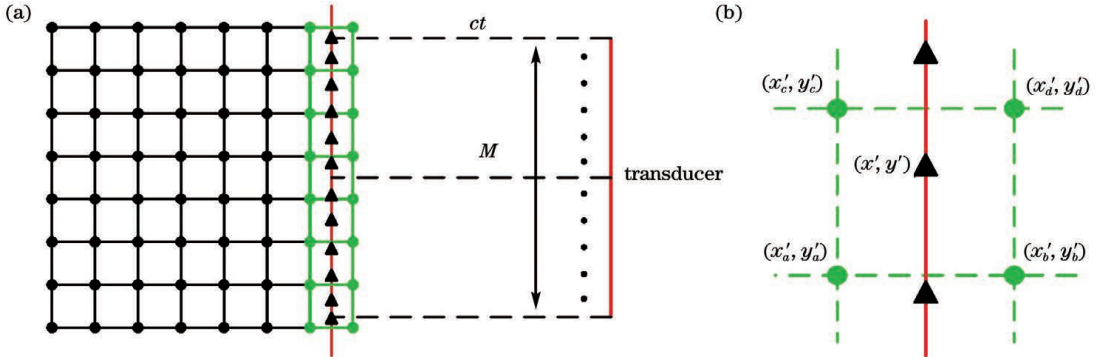

图 3　虚拟平行投影模型与线性插值模型。(a)MB-VP 对正向模型的离散化;(b)平行线各点与 4 个相邻点之间权重关系的插值示意图

Fig. 3　Models of virtual parallel-projection and linear interpolation. (a) Discretization of the forward model by MB-VP; (b) interpolation schematic of the weight between each point on parallel-projection line and four adjacent points

2.3 实验设计

为了验证虚拟平行投影光声模型重建方法的性能，首先设置半径为 200 μm 的多个微球进行数值模拟实验验证。采用所搭建的光声成像系统进行实验验证，仿体实验中采用直径为 200 μm 的聚乙烯微球作为成像目标体。用 30 mL 蒸馏水和 0.84 g 琼脂粉加热后冷却固化成圆柱状仿体，并在其表面的不同位置镶嵌聚乙烯微球，并保证距旋转中心不同位置处均有微球存在。为了进一步验证该虚拟平行投影光声模型重建算法对活体小动物成像的可行性，对体重约为 18.4 g 的四周龄昆明鼠胸腔部位进行光声成像实验。实验前，去除小鼠的毛发，以减小其对成像结果的干扰，然后用质量分数为 10% 的水合氯醛溶液对小鼠进行腹腔麻醉，并将其固定在成像腔中。成像过程中的水温保持在 33 ℃左右，成像完成后将活体小鼠取出。

3 分析与讨论

3.1 数值模拟

数值模拟验证被用来评估该方法的重建性能。设置了 4 个半径为 200 μm 的微球，其与旋转中心之间的距离分别为 0，3，6，9 mm。探测器中心距旋转中心的距离为 80 mm，探测到信号后，探测器以 1°为间隔角旋转一周完成光声信号的采集。探测器晶面剖分为 800 个离散点元，将每个离散点获得的光声信号累加求和并将求和结果作为整个探测器接收的光声信号。图 4(a)～(d)分别为原始图像及 MB、MB-SE 和 MB-VP 方法的重建结果。三种重建方法的 LSQR 迭代次数均设置为 5，数值模拟的重建网格数为 400×400。

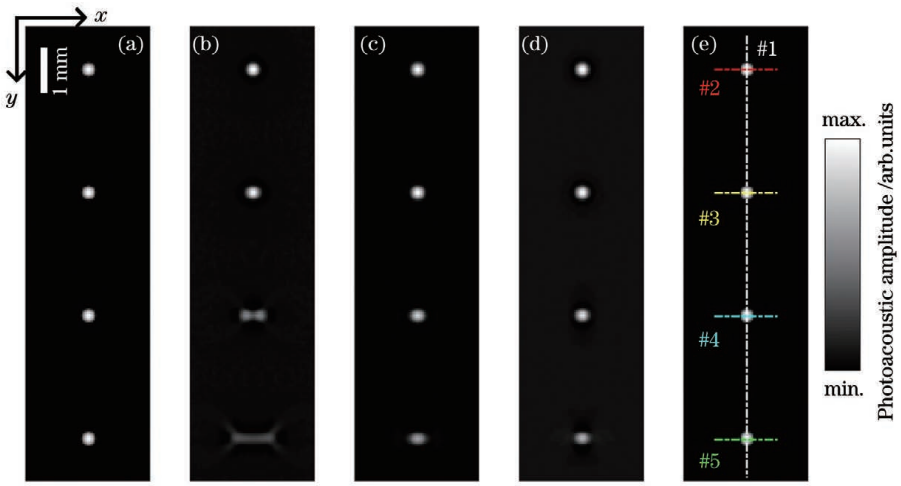

图 4 数值模拟结果。(a)原始图像；(b)MB 方法的重建结果；(c)MB-SE 方法的重建结果；(d)MB-VP 方法的重建结果；(e)轮廓强度剖线

Fig. 4 Results of numerical simulation. (a) Exact image; (b) reconstructed result by MB method; (c) reconstructed result by MB-SE method; (d) reconstructed result by MB-VP method; (e) profile line

从图 4 中可以看出，对于远离扫描中心（y 轴方向）位置的第 3、第 4 个微球，传统 MB 方法的重建结果明显失真，而 MB-SE 和 MB-VP 方法均可以准确重建出微球的形状。为了更好地定量分析不同方法的重建结果，取图 4(e)中＃1～＃5 指示线的剖线图（如图 5 所示）进行分析。剖线图的分析结果表明，MB 方法重建结果中的幅值随着到扫描中心距离的增加而急剧减小，MB-SE 和 MB-VP 重建结果中的幅值也有相同的趋势变化，但变化量较小，其中 MB-VP 的幅值最接近真实结果。表 1 中列出了 4 个微球的半峰全宽（FWHM），与 MB 和 MB-SE 方法相比，MB-VP 方法得到的 FWHM 最接近真实值。

表 1 沿 x 轴方向 4 个微球的 FWHM

Table 1 FWHM of four microspheres along x-axis

No.	FWHM /μm			
	Exact	MB	MB-SE	MB-VP
＃2	278	267	275	275
＃3	278	288	285	280
＃4	278	645	317	297
＃5	278	1104	391	344

为了直观地比较 MB-VP 和 MB-SE 方法在建模时间与内存消耗上的差异，将重建网格减小至 256×256。在 MB-SE 方法中，分别将探测器晶面剖分为 7、9、11、13、15 个离散点，运行时间和内存占用情况如表 2 所示。MB-VP 方法不需要剖分晶面，

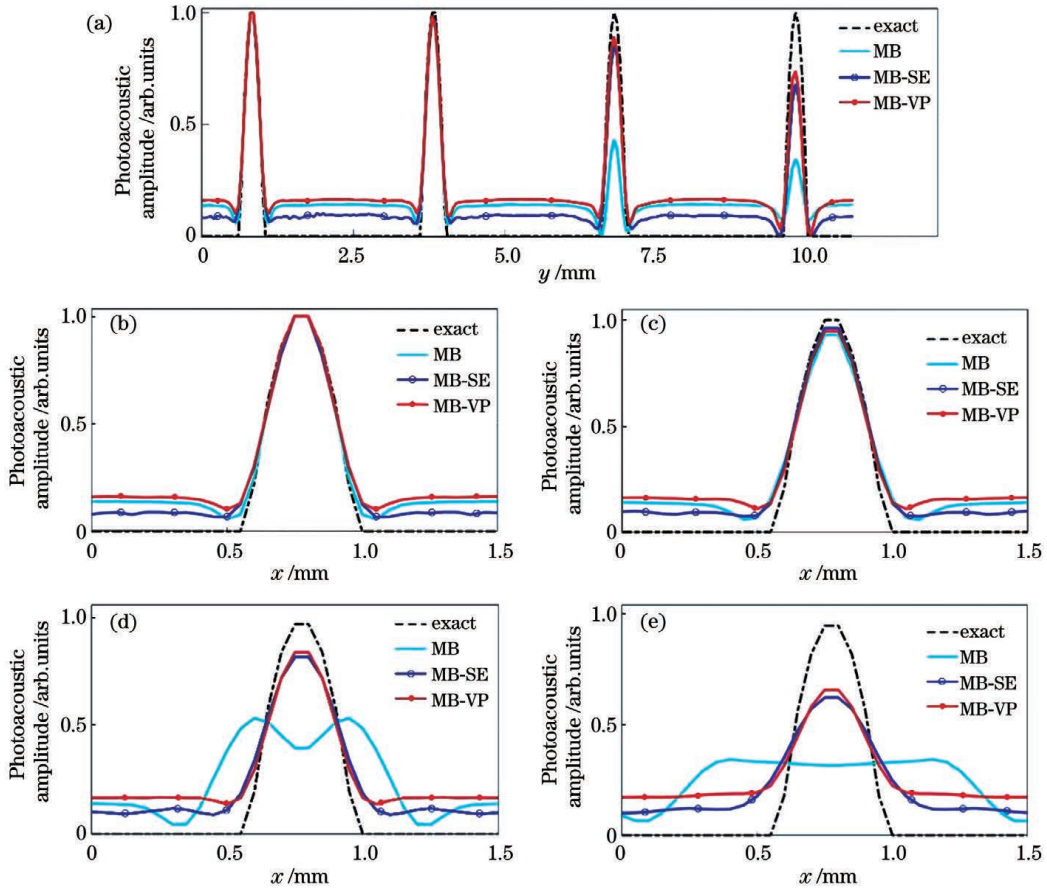

图 5　沿图 4(e)中＃1～＃5 指示线的剖线图。(a)沿＃1 虚线的剖线图;(b)～(e)沿＃2～＃5 虚线的剖线图

Fig. 5　Profiles along ＃1, ＃2, ＃3, ＃4, and ＃5 lines in Fig. 4(e). (a) Profile along ＃1 line; (b)-(e) profiles along ＃2, ＃3, ＃4, and ＃5 lines

表 2　MB-SE 方法和 MB-VP 方法的建模成本差异

Table 2　Difference in modeling costs of MB-SE and MB-VP methods

Computing cost	MB-SE	MB-SE	MB-SE	MB-SE	MB-SE	MB-VP
Element	7	9	11	13	15	–
Memory /GB	8.71	10.35	11.83	13.19	14.44	1.59
Run-time /s	262.13	341.14	420.09	499.38	737.20	39.29

计算时间仅约为 39 s,内存占用约 1.6 GB。MB-SE 方法的时间消耗和计算/存储空间需求随晶面离散点剖分数目的增加而线性增大,当探测器晶面被离散为 15 个点时,计算时间超过了 10 min,大约为 MB-VP 方法的 20 倍。如果继续增加探测器离散点的数目,如增至 800 个离散点,或者加密重建网格,则重建时间将近甚至超过 10 h,此时的时间消耗及计算/存储空间需求使得 MB-SE 重建方法不具有使用价值。取一个距扫描中心为 6 mm 的微球的 MB-SE 方法的重建图像进行放大显示,显示结果及中心剖线图如图 6 所示。从图 6 中可以看出:探测器晶面剖分为 7 个离散点时,微球的重建图像中存在明显的伪影;当探测器晶面上的离散点增加到 15 个时,重建图像的伪影能够得到有效抑制,并且空间分辨率有所提高。数值模拟实验结果表明,MB-SE 方法需要增加探测器晶面离散点的个数,即在牺牲重建时间和内存的前提下,才能获得理想的重建结果,而 MB-VP 方法可以在保证图像质量的前提下减少重建时间和内存消耗。

3.2　仿体实验

对内含直径为 200 μm 聚乙烯微球的琼脂仿体进行成像实验,实验中的激光波长设置为 705 nm,重建结果如图7所示。在MB方法的重建图像中有

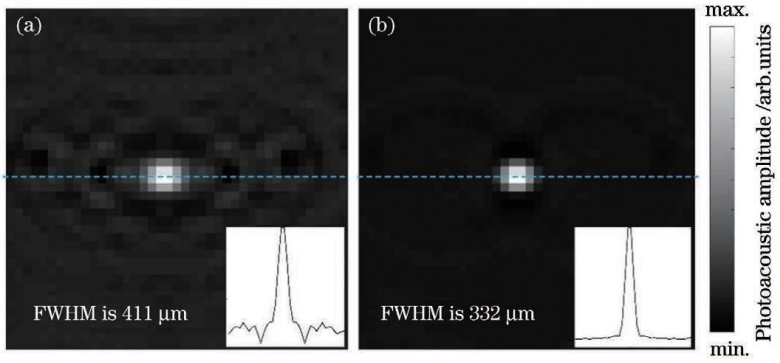

图 6　与扫描中心相距 6 mm 的微球的 MB-SE 重建图像。(a)晶面离散为 7 个离散点;(b)晶面离散为 15 个离散点

Fig. 6　MB-SE reconstructed images of microsphere with a distance of 6 mm from the center. (a) Seven surface elements; (b) fifteen surface elements

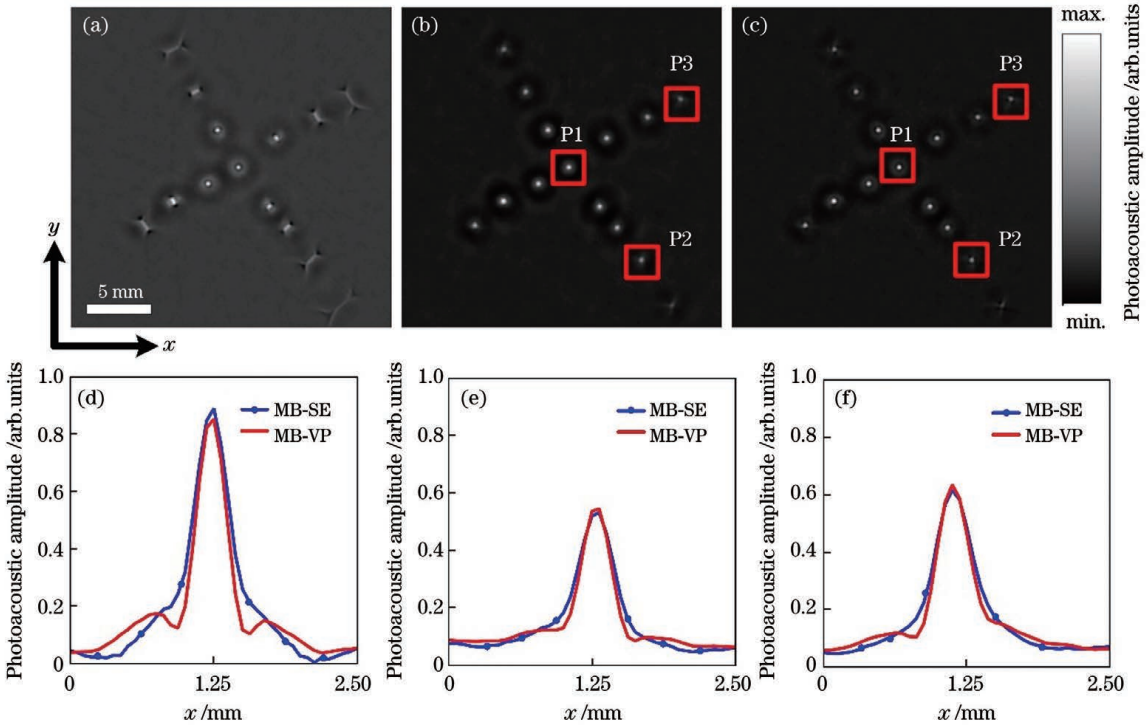

图 7　仿体实验结果。(a)MB 重建结果;(b)MB-SE 重建结果;(c)MB-VP 重建结果;(d)～(f)分别为 P1、P2 和 P3 沿 x 轴的剖线图

Fig. 7　Experimental results of phantom. (a) Reconstructed result by MB; (b) reconstructed result by MB-SE; (c) reconstructed result by MB-VP; (d)-(f) profiles of P1, P2, and P3 along x-axis, respectively

明显的背景噪声,且远离扫描中心位置处的微球出现了失真,而 MB-VP 和 MB-SE 方法均能够有效地抑制背景噪声并恢复出微球的真实形状,得到保真度高的重建图像,这与数值模拟实验的结果一致。MB-VP 与 MB-SE 方法重建图像中距扫描中心不同位置处的三个微球(P1～P3)的剖线图(沿 x 轴)如图 7(d)～(f)所示,微球的 FWHM 如表 3 所示。MB-SE 方法重建图像中三个微球 P1～P3 的 FWHM 分别为 345,352,373 μm,MB-VP 方法重建图像中三个微球 P1～P3 的 FWHM 分别为 294,295,362 μm。

表 3　仿体实验中微球的 FWHM

Table 3　FWHM of microspheres in phantom experiments

Microspheres No.	FWHM /μm	
	MB-SE	MB-VP
P1	345	294
P2	352	295
P3	373	362

3.3　动物实验

为了进一步验证虚拟平行投影模型重建方法在生物医学应用中的可行性,采用 850 nm 波长的激发

光对约 18.4 g 的健康昆明鼠胸腔区域进行成像，重建前采用 12 MHz 的截止频率对采集的信号进行低通滤波，三种方法的 LSQR 迭代次数均设置为 3，得到的重建结果如图 8 所示。在三种重建方法的实验结果中均可以明显看到下腔静脉（IVC）、门静脉（PV）、腹主动脉（AA）及光吸收较弱的脊柱（VE）等标志性解剖结构。在远离扫描中心的小鼠表皮位置处，MB 方法重建的边缘血管的结构、形状存在失真（如图中箭头所示），而这些血管在 MB-SE 和 MB-VP 方法的重建图像中获得了高保真度的还原。对比图 8(a)～(c)中虚线框区域内结构的放大图像可以发现，MB 方法重建结果的对比度较低，无法准确地从背景中判别有效信息，而在 MB-SE 和 MB-VP 方法的重建图像中可以看到细微的血管网络，重建图像具有较高的分辨率。实验结果表明，MB-VP 方法适用于活体小动物成像，且与 MB-SE 方法具有相似的重建性能。

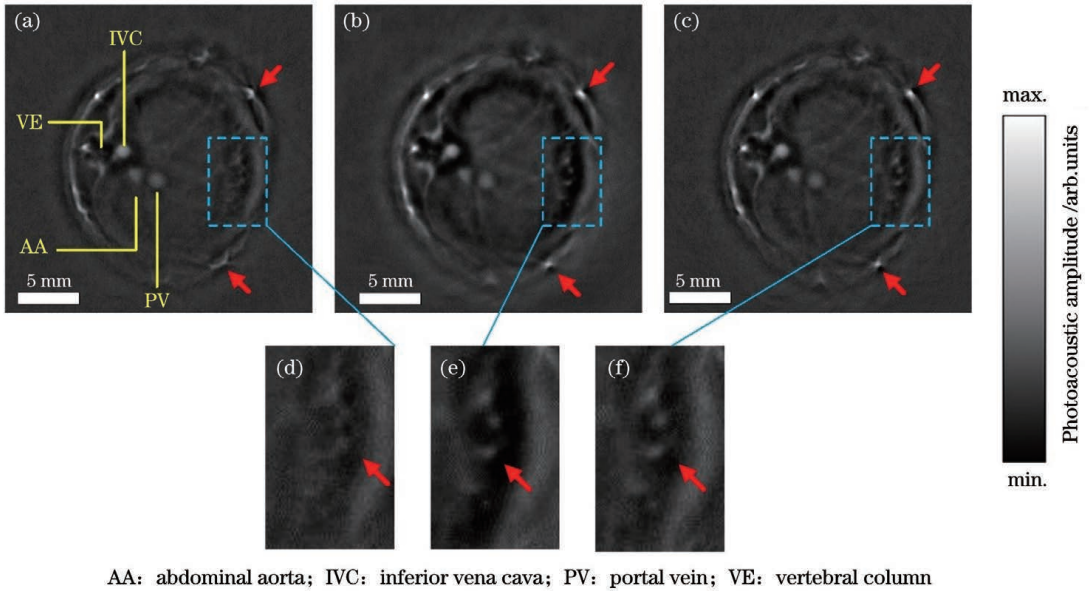

图 8 活体小鼠实验重建结果。(a) MB；(b) MB-SE；(c) MB-VP；(d)～(f)虚线框区域的放大图像

Fig. 8 Reconstructed results of *in vivo* mouse. (a) MB; (b) MB-SE; (c) MB-VP; (d)–(f) zoom-in images of the dotted rectangular areas

4 结 论

本文提出了一种基于虚拟平行投影的光声模型重建（MB-VP）方法，该方法可保证采用大晶面柱形聚焦或平面超声换能器的 PAT 成像系统快速准确地构建正向模型矩阵，解决了传统离散近似模型重建算法存在的计算时间及计算/存储空间消耗大、计算精度与计算效率相矛盾等问题。通过数值模拟、仿体实验和小鼠活体实验对所提算法的重建性能进行了评估，结果证明了该方法可以在保证最佳重建图像质量的前提下有效降低计算成本，即 MB-VP 方法可以获得与 MB-SE 方法相同的高质量、高保真度重建图像，同时，MB-VP 的计算成本仅近似于经典的 MB 方法。所提模型重建算法可以进一步通过基于 GPU 加速的并行计算方法提高计算效率，从而达到实时成像的要求。

参 考 文 献

[1] Manohar S, Razansky D. Photoacoustics: a historical review[J]. Advances in Optics and Photonics, 2016, 8(4): 586-617.

[2] Lu T, Gao F, Song S Z, et al. Tumor-specific imaging of small animals based on multi-angle optoacoustic mesoscopy imaging method[J]. Chinese Journal of Lasers, 2020, 47(2): 0207032.
路彤, 高峰, 宋少泽, 等. 基于多角度光声介观成像方法的小动物肿瘤特异性成像[J]. 中国激光, 2020, 47(2): 0207032.

[3] Taruttis A, Ntziachristos V. Advances in real-time multispectral optoacoustic imaging and its applications [J]. Nature Photonics, 2015, 9(4): 219-227.

[4] Liu Q, Jin T, Chen Q, et al. Research progress of miniaturized photoacoustic imaging technology in biomedical field[J]. Chinese Journal of Lasers, 2020, 47(2): 0207019.
刘强, 金天, 陈倩, 等. 小型化光声成像技术在生物医学领域的研究进展[J]. 中国激光, 2020, 47(2): 0207019.

[5] Zhang G P, Deng L J, Bai Y, et al. Recent advances in photoacoustic tomography based on circular array

transducer[J]. Laser & Optoelectronics Progress, 2020, 57(12): 120004.
张国鹏, 邓丽军, 白杨, 等. 基于环形阵列式传感器的光声层析成像研究进展[J]. 激光与光电子学进展, 2020, 57(12): 120004.

[6] Wang L V, Yao J. A practical guide to photoacoustic tomography in the life sciences[J]. Nature Methods, 2016, 13(8): 627-638.

[7] Wang X, Pang Y, Ku G, et al. Noninvasive laser-induced photoacoustic tomography for structural and functional *in vivo* imaging of the brain[J]. Nature Biotechnology, 2003, 21(7): 803-806.

[8] Toi M, Asao Y, Matsumoto Y, et al. Visualization of tumor-related blood vessels in human breast by photoacoustic imaging system with a hemispherical detector array[J]. Scientific Reports, 2017, 7: 41970.

[9] Butler R, Lavin P T, Tucker F L, et al. Optoacoustic breast imaging: imaging-pathology correlation of optoacoustic features in benign and malignant breast masses[J]. American Journal of Roentgenology, 2018, 211(5): 1155-1170.

[10] Sun Y, Sobel E, Jiang H. Quantitative three-dimensional photoacoustic tomography of the finger joints: an *in vivo* study[J]. Journal of Biomedical Optics, 2009, 14(6): 064002.

[11] Sun Y, Sobel E S, Jiang H. First assessment of three-dimensional quantitative photoacoustic tomography for *in vivo* detection of osteoarthritis in the finger joints[J]. Medical Physics, 2011, 38(7): 4009-4017.

[12] Tzoumas S, Nunes A, Olefir I, et al. Eigenspectra optoacoustic tomography achieves quantitative blood oxygenation imaging deep in tissues[J]. Nature Communications, 2016, 7: 12121.

[13] Ntziachristos V, Razansky D. Molecular imaging by means of multispectral optoacoustic tomography (MSOT)[J]. Chemical Reviews, 2010, 110(5): 2783-2794.

[14] Taruttis A, Morscher S, Burton N C, et al. Fast multispectral optoacoustic tomography (MSOT) for dynamic imaging of pharmacokinetics and biodistribution in multiple organs[J]. PLoS One, 2012, 7(1): e30491.

[15] Queirós D, Déan-Ben X L, Buehler A, et al. Modeling the shape of cylindrically focused transducers in three-dimensional optoacoustic tomography[J]. Journal of Biomedical Optics, 2013, 18(7): 076014.

[16] Dean-Ben X L, Ntziachristos V, Razansky D. Acceleration of optoacoustic model-based reconstruction using angular image discretization[J]. IEEE Transactions on Medical Imaging, 2012, 31(5): 1154-1162.

[17] Dean-Ben X L, Buehler A, Ntziachristos V, et al. Accurate model-based reconstruction algorithm for three-dimensional optoacoustic tomography[J]. IEEE Transactions on Medical Imaging, 2012, 31(10): 1922-1928.

[18] Pramanik M. Improving tangential resolution with a modified delay-and-sum reconstruction algorithm inphotoacoustic and thermoacoustic tomography[J]. Journal of the Optical Society of America A, Optics, Image Science, and Vision, 2014, 31(3): 621-627.

[19] Ding L, Deán-Ben X L, Razansky D. Real-time model-based inversion in cross-sectional optoacoustic tomography[J]. IEEE Transactions on Medical Imaging, 2016, 35(8): 1883-1891.

[20] Ding L, Deán-Ben X L, Razansky D. Efficient 3-D model-based reconstruction scheme for arbitrary optoacoustic acquisition geometries[J]. IEEE Transactions on Medical Imaging, 2017, 36(9): 1858-1867.

[21] Lutzweiler C, Deán-Ben X L, Razansky D. Expediting model-based optoacoustic reconstructions with tomographic symmetries[J]. Medical Physics, 2014, 41(1): 013302.

[22] Wang K, Ermilov S A, Su R, et al. An imaging model incorporating ultrasonic transducer properties for three-dimensional optoacoustic tomography[J]. IEEE Transactions on Medical Imaging, 2011, 30(2): 203-214.

[23] Rosenthal A, Ntziachristos V, Razansky D. Model-based optoacoustic inversion with arbitrary-shape detectors[J]. Medical Physics, 2011, 38(7): 4285-4295.

[24] Cox B T, Kara S, Arridge S R, et al. k-space propagation models for acoustically heterogeneous media: application to biomedical photoacoustics[J]. Journal of the Acoustical Society of America, 2007, 121(6): 3453-3464.

[25] Araque Caballero M Á, Gateau J, Déan-Ben X L, et al. Model-based optoacoustic image reconstruction of large three-dimensional tomographic datasets acquired with an array of directional detectors[J]. IEEE Transactions on Medical Imaging, 2014, 33(2): 433-443.

[26] Wang Y H, Lu T, Li J, et al. Enhancing sparse-view photoacoustic tomography with combined virtually parallel projecting and spatially adaptive filtering[J]. Biomedical Optics Express, 2018, 9(9): 4569-4587.

Reconstruction Algorithm Based on a Virtual Parallel-Projection Model for Photoacoustic Tomography Using an Ultrasonic Transducer with a Large Active Surface

Li Jiao[1,2*], Miao Shichao[1], Song Shaoze[1], Lu Tong[1], Chen Tingting[1], Gao Feng[1,2]

[1] *College of Precision Instruments and Opto-Electronic Engineering, Tianjin University, Tianjin 300072, China*;

[2] *Tianjin Key Laboratory of Biomedical Detecting Techniques and Instruments, Tianjin 300072, China*

Abstract

Objective In photoacoustic tomography, considering the size of ultrasonic transducers, especially for ones with large active surfaces, the traditional model-based (MB) method sums up the forward model matrix of each discrete point from the active surface to build this matrix. Although this traditional method has greater accuracy than the delay-and-sum method and back-projection method, with an increase in the number of discrete points from the active surface of transducer, the computing time and memory consumption will be more. Here, we present a new MB photoacoustic reconstruction algorithm based on the concept of virtual parallel projection. This model is suitable for photoacoustic tomography systems employing flat or cylindrical focused transducers with large active surfaces. This reconstruction algorithm directly establishes a virtual parallel-projection model matrix to replace the sum of the model matrices of the discrete points of the surface. The proposed method has an image performance similar to that of the traditional MB reconstruction method with discretized surface elements but considerably lower time consumption and storage requirements in the reconstruction process. We hope that this high-efficiency, high-accuracy method can provide a valuable reference and guidance for the research on MB photoacoustic reconstruction algorithms for use in real-time photoacoustic tomography.

Methods A photoacoustic reconstruction algorithm based on a virtual parallel-projection model is introduced to solve the problem caused by transducers with large active surfaces. When the distance between the image center and transducer satisfies the virtual parallel-projection condition (Eq. 6), the back-projection profile of each discrete point on the active surface in the reconstruction area can be approximated as a straight line parallel to the transducer (Fig. 3). Then, a virtual parallel-projection model matrix can be directly built to replace the sum of the model matrices based on all discrete points on the surface. This step helps avoid the repeated matrix calculations of each discrete point and can reduce the time and memory requirements. The image performance of the proposed method was first demonstrated by numerical simulation using microspheres with a radius of 200 μm. We compared the photoacoustic images reconstructed by three methods, namely, the traditional model-based (MB) method, MB method with discrete surface elements (MB-SE), and proposed method based on virtual parallel-projection (MB-VP). The computing time and memory consumption of MB-SE and MB-VP methods were quantitatively calculated to show the high efficiency of the proposed method. Then, the phantom experiment was implemented using a self-built photoacoustic imaging system to verify the reconstructed accuracy of the MB-VP method (Fig. 1). This agar phantom consisted of some polyethylene microspheres of diameter 200 μm. These microspheres were approximately embedded on the same plane in the phantom. Finally, to assess the feasibility of the MB-VP method for *in vivo* imaging, animal experiments were performed on the thoracic cavity region of a four-week-old KM mouse (~18.4 g).

Results and Discussions The reconstruction results of the proposed MB-VP method show high image quality and high reconstruction accuracy, comparable to those of the MB-SE method (Fig. 4). However, the MB-SE method obtains desirable reconstruction results at the expense of computing time and memory consumption by increasing the number of discrete points on the active surface of the transducer (Table 2). When the active surface of the transducer is discretized into 15 points for the MB-SE method, the calculation time exceeds 10 min, which is approximately 20 times that of the proposed MB-VP method. In contrast, the MB-VP method provides higher quality and better spatial resolution in the reconstructed image with significantly lower reconstruction time and memory consumption (Fig. 6). The phantom experiment results, which are consistent with the numerical simulation results, demonstrate that both MB-VP and MB-SE methods can effectively suppress image artifacts and obtain high-fidelity

reconstructed images (Fig. 7 and Table 3). The animal experiment results show that the result of the MB method suffers from artifacts and distortions, especially in the imaging of blood vessels at the position of the mouse epidermis far away from the image center; in contrast, the shapes of these blood vessels are accurately recovered by the MB-SE and MB-VP methods (Fig. 8).

Conclusions In this work, a novel MB reconstruction algorithm based on the concept of virtual parallel-projection is developed to achieve high-efficiency MB reconstructions for photoacoustic tomography employing flat or cylindrical focused transducers with large active surfaces. By quickly and accurately building the forward model matrix based on the virtual parallel-projection condition, the proposed method can break the trade-off between reconstructed accuracy and computing consumption, which limits the applications of the traditional MB reconstruction methods. The results of numerical simulations, phantom experiments, and *in vivo* experiments demonstrate that the execution time and memory space required to reconstruct the initial pressure image are considerably reduced by the proposed method without sacrificing the quality of the reconstructed images. In other words, the MB-VP and MB-SE methods can obtain similar reconstructed images with higher quality and higher fidelity than the MB method, while the computational cost of the MB-VP method similar to that of the MB method, that is, it is much lower than that of the MB-SE method. The computational efficiency of the proposed method can be further improved through the parallel computation approach based on graphics processing unit acceleration to meet the requirements of real-time photoacoustic tomography.

Key words medical optics; photoacoustic tomography; virtual parallel-projection; model-based reconstruction algorithm

OCIS codes 170.5120; 110.5120; 110.3010